Autonomous Robots manuscript No.
(will be inserted by the editor)

Neuromuscular Model Achieving Speed Control and Steering with a 3D Bipedal Walker

Nicolas Van der Noot · Auke Jan Ijspeert · Renaud Ronsse

Received: date / Accepted: date

Abstract Nowadays, very few humanoid robots manage to travel in our daily environments. This is mainly due to their limited locomotion capabilities, far from the human ones. Recently, we developed a bio-inspired torque-based controller recruiting virtual muscles driven by reflexes and a central pattern generator. Straight walking experiments were obtained in a 3D simulation environment, resulting in the emergence of human-like and robust gait patterns, with speed modulation capabilities. In this paper, we extend this model, in order to control the steering direction and curvature. Based on human turning strategies, new control pathways are introduced and optimized to reach the sharpest possible turns. In sum, tele-operated motions can be achieved through the control of two scalar inputs (i.e. forward speed and heading). This is particularly relevant for steering the robot on-line, and navigating in cluttered environments. Finally, the biped demonstrated significant robustness during blind walking experiments.

This research was supported by the Belgian F.R.S.-FNRS (Aspirant #16744574 awarded to NVdN) and by the European Community's Seventh Framework Programme under Grant 611832 (WALK-MAN).

N. Van der Noot
Center for Research in Mechatronics, Institute of Mechanics, Materials and Civil Engineering, Université catholique de Louvain, B-1348 Louvain-la-Neuve
Tel.: +32 10 47 25 09
E-mail: nicolas.vandernoot@uclouvain.be

A. J. Ijspeert
Biorobotics Laboratory, Institute of Bioengineering, École Polytechnique Fédérale de Lausanne, CH-1015 Lausanne, Switzerland
E-mail: auke.ijspeert@epfl.ch

R. Ronsse
Center for Research in Mechatronics, Institute of Mechanics, Materials and Civil Engineering, Université catholique de Louvain, B-1348 Louvain-la-Neuve E-mail: renaud.ronsse@uclouvain.be

Keywords Biologically-Inspired Robots · Humanoid Robots · Legged Robots · Motion Control · Curved Walking

1 Introduction

Nowadays, there is an increasing interest in bringing mobile robots in our everyday life. However, their mobility, usually different from ours, restricts them to move in dedicated environments. In contrast, humanoid robots are potentially adapted to move in environments designed for humans, since their body is very similar to the human one (Schaal, 2007). Moreover, their morphology offers the possibility to manipulate tools fitting human dexterity. Therefore, these tools do not require to be adapted to the robot needs, favoring potential co-operative work with humans (Fitzpatrick et al, 2016).

However, navigation in the unpredictable human world remains an important issue, as emphasized during the recent DARPA Robotics Challenge (Johnson et al, 2016). In particular, robot's locomotion skills are far from reaching the level of the human ones, therefore usually restricting them to move in controlled environments, such as laboratories. Most popular biped locomotion algorithms recruit the zero-moment point (ZMP) as an indicator of gait feasibility, in order to guarantee dynamic stability at every moment during locomotion (Vukobratovic and Borovac, 2004). Many successful walking experiments were conducted using this indicator, for instance with ASIMO (Chestnutt et al, 2005) or with the HRP-2 platform (Kaneko et al, 2002).

Interestingly, these methods can offer a mathematical framework for postural control and steering, for example through appropriate footstep planner strategies recruiting inverse kinematics or dynamics (Faraji et al, 2014). However, common drawbacks associated with most ZMP-based bipedal controllers include energy inefficiency, unnatural gait (low

waist position, continuous knee bending, feet kept parallel to the ground, etc.), poor resistance to modeling errors or external perturbations and slow walking speeds (Sardain and Bessonnet, 2004; Kurazume et al, 2005; Dallali, 2011).

In contrast, the limit cycle concept relaxes constraints inherent to the ZMP criterion, by focusing on global stability during walking, instead of local stability at every moment of the gait (Hobbelen and Wisse, 2007). Successful implementations of this concept include the (quasi-)passive walkers, resulting in efficient human-like gaits (McGeer, 1990; Collins and Ruina, 2005; Hobbelen et al, 2008). However, gait modulation is usually very limited, due to the lack of control parameters.

Bio-inspired controllers are emerging as a promising way to implement adaptive limit-cycle walking, by designing control strategies based on concepts identified in humans. In particular, the neuromuscular model developed in (Geyer and Herr, 2010) - and further extended in (Song and Geyer, 2015) - can generate robust human-like walking through the recruitment of muscles controlled by reflexes. Experimental validations of this approach include the control of a powered ankle-foot prosthesis (Eilenberg et al, 2010) and the locomotion of a humanoid robot in 2D, i.e. when assistance was provided to the lateral balance (Van der Noot et al, 2015a).

In contrast to inverse kinematics/dynamics approaches, the gait modulation and steering of these bio-inspired approaches remain challenging, due to the lack of straightforward mathematical framework. In (Desai and Geyer, 2013), the reflex rules of (Geyer and Herr, 2010) were extended to control the swing leg placement. Another avenue to modulate the gait is through the introduction of a central pattern generator (CPG). CPGs are neural circuits capable of producing rhythmic patterns of neural activity without receiving rhythmic inputs. They display valuable features among which the possibility to modulate locomotion with simple low-dimensional control signals (Ijspeert, 2008).

While locomotor CPGs were identified in many vertebrates, their involvement in human locomotion is still a matter open to debate (Minassian et al, 2017). In particular, human-like gaits can be achieved using computational models, both with and without CPG. Successful CPG implementations include the robust bipedal walking experiments of (Aoi and Tsuchiya, 2005) by means of nonlinear oscillators, the adaptation of a biped locomotion on uneven terrains using CPG modulation (Taga, 1994), and the development of a neuromuscular model recruiting a CPG as central element, in order to investigate the effects of a spinal cord injury on locomotor abilities (Paul et al, 2005).

In (Van der Noot et al, 2015b), we designed a 2D locomotion algorithm, combining a CPG and reflexes in a neuromuscular torque-based controller. This is coherent with Kuo's framework, suggesting to combine feedback (i.e. reflexes) and feed-forward (i.e. CPG) pathways in the control of a periodic task (Kuo, 2002). We recently incremented this latest controller in (Van der Noot et al, 2018), in order to provide lateral balance, and thus to walk in 3D environments. After a single off-line optimization process, our controller could generate energy-efficient and human-like straight-walking gaits (both regarding kinematics and dynamics). Using a simulated COMAN platform (a 95 cm tall humanoid robot) as embodiment, the forward speed could be continuously commanded from 0.4 to $0.9\,m/s$. This range is close to the healthy human one, once scaled to the robot size. This speed modulation was achieved by changing high-level parameters, as linear or quadratic functions of the target speed.

The present contribution builds on top of this bio-inspired controller, by extending the 3D straight-walking gaits to achieve control of the turning direction. More precisely, the CPG and reflex rules developed in (Van der Noot et al, 2018) are adapted to control both the forward speed and the path curvature (direction and curvature). This is particularly relevant in tele-operation scenarios where the robot has to move in a cluttered environment. Similarly to the existing speed controller, the turning modulation is achieved by controlling a scalar input (i.e. the heading reference), together with the adaptation of high-level parameters, as linear or quadratic functions of the speed reference.

This paper is divided as follows. Section 2 summarizes the neuromuscular controller developed in (Van der Noot et al, 2018), achieving straight walking and forward speed modulation. That section also reports the simulation environment and the COMAN platform embodying our controller. The straight walking controller is later incremented in Section 3, in order to achieve the control of the steering direction. This additional steering control is further studied in Section 4, with focus on adaptation to different walking speeds. Then, Section 5 analyses different features of the resulting steering motion, among which the achievable walking curvature, the biped robustness and some tele-operated scenarios. Finally, Section 6 concludes the paper.

2 Straight walking controller

Here, biped locomotion control is achieved using virtual muscles commanded by the combined action of reflexes and a central pattern generator (CPG). Using this approach, 3D straight walking with forward speed modulation can be achieved, as reported in (Van der Noot et al, 2018). The main principles governing this approach are outlined in this section.

2.1 Neuromuscular model

The walking controller generates torque references at the joint level by recruiting (virtual) muscles. The full muscular

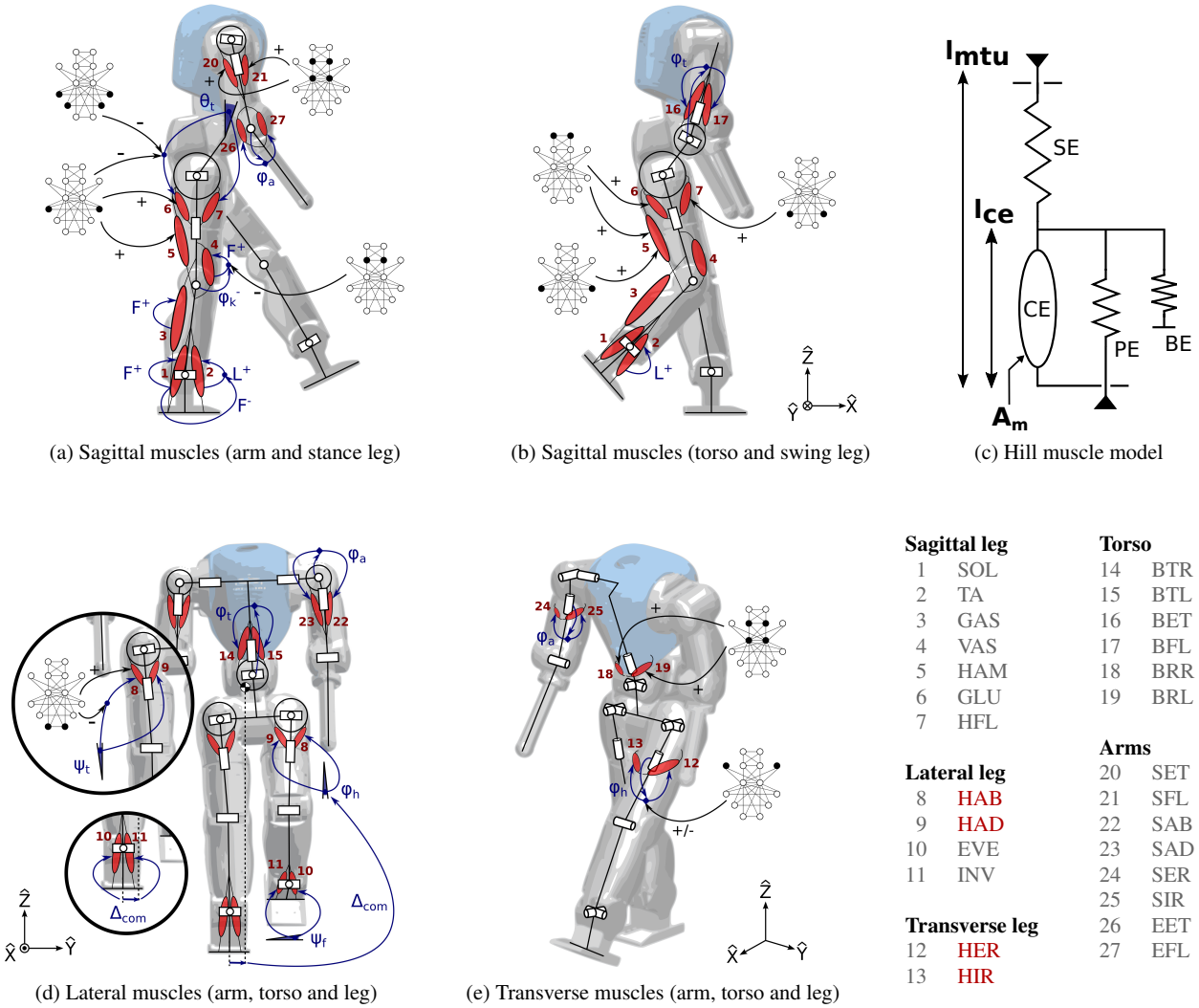

(a) Sagittal muscles (arm and stance leg)

(b) Sagittal muscles (torso and swing leg)

(c) Hill muscle model

(d) Lateral muscles (arm, torso and leg)

(e) Transverse muscles (arm, torso and leg)

Fig. 1 To actuate the biped's 23 joints, the controller recruits 27 different Hill muscle models (panel (c)) acting in different planes. These muscles are commanded by a combination of reflex signals and the CPG central unit. Muscles acting in the sagittal plane are displayed in panels (a) and (b), the ones acting in the lateral plane are displayed in panel (d), and finally, the ones acting in the transverse plane are depicted in panel (e). In particular, turning is mainly controlled by the HAB and HAD muscles in the lateral plane (panel (d)) and by the HER and HIR muscles in the transverse plane (panel (e)). The full muscle names are provided in (Van der Noot et al, 2018).

configuration is presented in Fig. 1 for the COMAN robot (Tsagarakis et al, 2013), which served as embodiment in our experiments (see Section 2.3). Each muscle is modeled as a set of equations based on a Hill muscle model (Hill, 1938), as depicted in Fig. 1c.

More precisely, each muscle tendon unit (MTU) consists of two main elements: a contractile element (CE) and a series elastic one (SE), capturing the tendon compliance. Two additional elements only engage when the muscle state is outside its normal range of operation: the parallel elastic (PE) and the buffer elastic (BE) elements. The MTU length l_{mtu} can be retrieved from geometric relationships, while the length of CE (l_{ce}) is obtained as the time-integral of its velocity v_{ce}. In turn, v_{ce} depends on l_{mtu} from force-length and -velocity relationships, and on the muscle activation A_m, detailed later. Then, the length l_{se} of SE (computed as $l_{mtu} - l_{ce}$) provides a direct computation of the muscle force. This force is later multiplied by a lever arm to generate a torque contribution at the joint level. Finally, the different torque contributions are summed and sent to the robot joint torque low-level controller. More information is provided in (Geyer and Herr, 2010) and (Van der Noot et al, 2018).

The muscle activations A_m are related to neural inputs S_m called stimulations, through the following excitation-contraction coupling first-order equation: $\tau_m \, dA_m/dt = S_m - A_m$, where

τ_m is a time constant of $10ms$. Actuating the muscles, and so controlling the whole biped locomotion, thus amounts to compute appropriate stimulations S_m.

2.2 Reflexes and central pattern generator

The neural stimulations S_m are computed as a combination of reflex mechanisms (feedback) and signals produced by a central pattern generator (CPG, feed-forward) (Rossignol et al, 2006). The combination of these two types of signals mainly follows a proximo-distal gradient. In other words, muscles close to the hips are mainly controlled by CPG signals, while the ones close to the feet (and so more impacted by external perturbations, like ground contact) are mainly driven by reflexes (Dzeladini et al, 2014; Daley et al, 2007).

All these reflexes and CPG inputs computations are fully detailed in (Van der Noot et al, 2018) and depicted in Fig. 1. For instance, in the stance phase, the soleus muscle (SOL) is stimulated with the following positive force feedback reflex: $G_{SOL}\tilde{F}_{SOL}$, where G_{SOL} is a fixed parameter and $\tilde{F}_{SOL}$ is the SOL muscle force normalized by its maximal force. Most of the reflexes - similar to the one here as example - are adapted from (Geyer and Herr, 2010).

For straight walking, the CPG was designed as a twelve-neurons network of Matsuoka oscillators (Matsuoka, 1985, 1987). These are bio-inspired artificial oscillators, capturing the mutual inhibition between half-centers located in the spinal cord. Each neuron N_i obeys the state equations provided in (1), where x_i is the firing rate, v_i is the self-inhibition modulated by an adaptation constant β_j, η_k are the mutual inhibition factors (captured by the function $[\bullet]^+ = max(0,\bullet)$) and u_i is the external input. Finally, τ is the time constant for the rate of discharge of x_i, while the one of the self-inhibition v_i is related to τ through the adimensional parameter γ_j.

$$\begin{aligned}\dot{x}_i &= \frac{1}{\tau}(-x_i - \beta_j v_i - \sum \eta_k [x_l]^+ + u_i) \\ \dot{v}_i &= \frac{1}{\gamma_j \tau}(-v_i + [x_i]^+)\end{aligned} \tag{1}$$

In Eq. (1), the index i corresponds to the neuron index, while the gains β_j, η_k, and the neurons x_l are specified in Fig. 3. Finally, γ_j takes the same index as β_j.

Furthermore, this CPG network was divided into two main parts. The first one, in charge of providing the main frequency and phasing during the gait, is composed of four neurons, i.e. the "rhythm generator" neurons (RG). They are denoted with a number (from 1 to 4), and depicted in Fig. 2a. The second layer relies on the RG neurons to generate signals shaping the patterns of muscle stimulations. The corresponding neurons are denoted with a letter (from A to H) and are called "pattern formations" neurons (PF). They are displayed in Fig. 2b. This two-layer structure is consistent with the two-level CPG biological structure proposed by (McCrea and Rybak, 2008) and validated during fictive locomotion experiments with decerebrated cats.

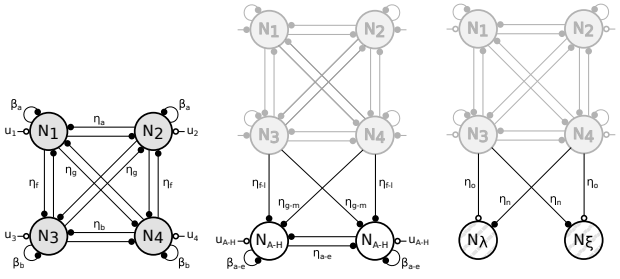

(a) RG neurons (b) PF neurons (c) TR neurons

Fig. 2 The CPG network is built by assembling three types of components: (a) the rhythm generator (RG) layer (four fully connected Matsuoka neurons), (b) a pair of pattern formation Matsuoka neurons (PF) driven by the RG neurons and (c) a pair of non-Matsuoka neurons controlling turning (TR), also driven by the RG neurons. The vertical symmetry corresponds to the left/right legs symmetry.

The full CPG network, for straight walking, is pictured in Fig. 3. The corresponding time-evolution of the neurons firing rates are displayed in Fig. 4. To generate the CPG contribution to a particular muscle stimulation S_m, different CPG outputs y_i were computed. They mainly consisted in extracting the positive firing rate of a PF neuron x_j (i.e. $y_i = [x_j]^+$). Then, the CPG contribution to a particular stimulation was computed as $S_m = \sum k_i y_i$, where k_i are gains. Again, all details about these computational steps are provided in (Van der Noot et al, 2018). In sum, Fig. 1 displays all CPG contributions to the actuation of the different muscles.

As detailed in (Van der Noot et al, 2018), nine key control parameters were identified to modulate the biped forward speed. More precisely, these parameters were adapted as linear or quadratic function of a scalar input: the speed reference v_{ref}, providing forward speed modulation in the range of $[0.4;0.9]\,m/s$.

2.3 Experimental embodiment

As embodiment for our experiments, we used the COmpliant huMANoid (COMAN) robotic platform, in the Robotran simulation environment. COMAN is a 23 degrees of freedom (DOFs) full-body humanoid robot developed at the Italian Institute of Technology (IIT) (Dallali et al, 2013; Tsagarakis et al, 2013). This 95 cm tall robot, weighting 31 kg, features both series elastic actuators (SEA) (Tsagarakis et al, 2009) (mainly for sagittal joints) and traditional, stiff actuators (for the other joints). Regarding the robot sensors, each joint features position encoders and custom-made torque sensors. On

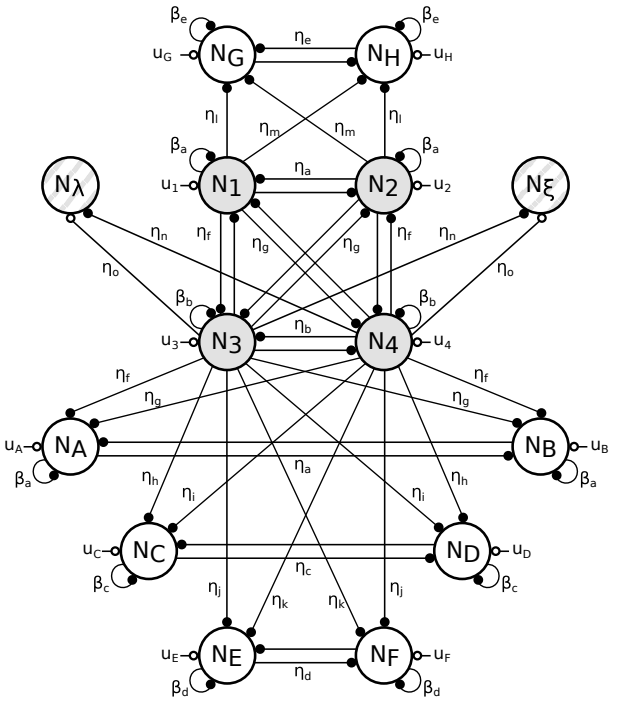

Fig. 3 The full CPG network is composed of the three components detailed in Fig. 2: (a) "rhythm generator" neurons (RG, shaded, N_{1-4}), (b) "pattern formation" ones (PF, N_{A-H}) and (c) "turning" ones (TR, hatched, $N_{\lambda,\xi}$). TR neurons obey Eq. (2), while the rest of the network is composed of Matsuoka oscillators, obeying Eq. (1). Inter-neuron excitations are indicated with an empty circle, while plain circles capture inhibitions. All neurons but N_λ and N_ξ were already used for straight walking, see (Van der Noot et al, 2018).

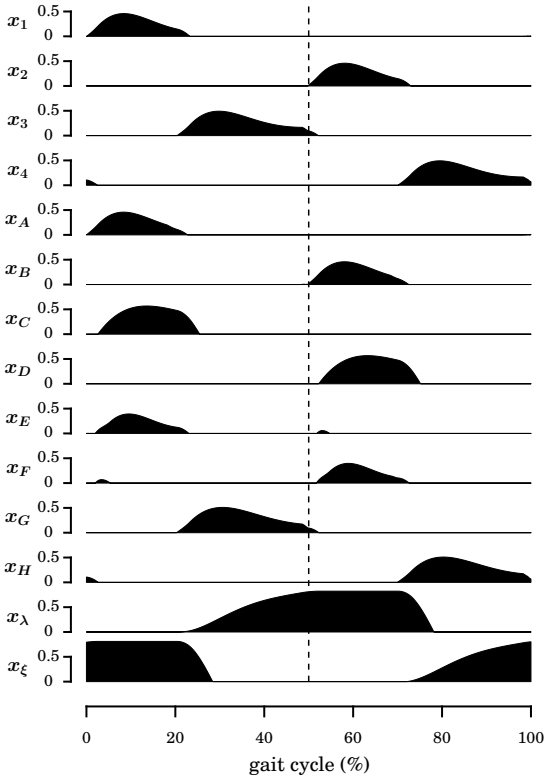

Fig. 4 Time-evolution of the 14 neurons firing rates of Fig. 3 over one gait cycle (0% and 100% correspond to consecutive right foot strikes, the dashed line corresponds to the left foot strike in-between). These signals are obtained during one typical gait cycle of the locomotion resulting from the controller used in all the results of this paper (called *reference controller*), with a speed reference of 0.65 m/s.

top of that, an inertial measurement unit (IMU) is attached to the robot waist, while custom-made 6 axis force/torque sensors are placed below the ankle joints.

The simulation suite used to model COMAN is called Robotran (Samin and Fisette, 2003; Docquier et al, 2013). It is a symbolic environment for multi-body systems developed within the Université catholique de Louvain. To further minimize the gap between simulation and reality, a particular attention was paid to capture proper actuator dynamics and external forces from the environment, in particular with the ground contact model (GCM). Moreover, only sensory signals available on the real robot were used. On top of that, a uniform noise with a maximal amplitude of $0.4Nm$ was added to the torque measurement, to reproduce the one measured with the real platform. The motor equations, coupled to this noise, generate actual joint torques being different from their references, as would happen with the real robot. The integration was performed using a Runge-Kutta integration scheme with a $250\mu s$ time step. COMAN, in its simulation environment, is visible in Fig. 1. More information about the robot and its simulator is provided in (Zobova et al, 2017; Van der Noot et al, 2018).

3 Extension to curved motion

The controller outlined in Section 2 and fully detailed in (Van der Noot et al, 2018) achieved straight walking in a 3D environment. In particular, forward speed modulation was achieved by adapting the speed reference v_{ref}, i.e. the main input of this bio-inspired controller. Building on top of this former contribution, this section introduces new features in order to achieve the control of the steering direction (curvature).

3.1 Lateral hip control

In (Courtine et al, 2006), ten healthy male adults walked along straight and curved paths while kinematics and electromyographic (EMG) data were recorded. A critical observation was that walking along curved paths did not require a dramatic re-organization of the basic EMG patterns required for walking straight-ahead. Inspired by this observation, the mechanisms governing the stimulation computations for straight walking described in Section 2 were mostly kept intact for curved motion. For most of them, changes in

steady-state profile would thus be the result of the interplay between reflexes, CPG signals and the environment.

In this contribution, the turning motion is controlled by a scalar reference: the heading reference h_{ref}, bounded in the $[-1;1]$ interval during on-line control (with -1 corresponding to maximal left curvature, 0 to straight motion and 1 to maximal right curvature). This value is used at each strike to compute two turning control signals. At each right strike, the left turning command is updated as $\Gamma_L = [h_{ref}]^-$ (with $[\bullet]^- = -min(\bullet,0)$). Similarly, the right turning command is updated as $\Gamma_R = [h_{ref}]^+$ at each left strike.

The curved motion mainly emerges from the foot transverse orientation control (detailed in Section 3.2). However, the body center of mass (COM) must also be controlled in the lateral plane, as mentioned in (Patla et al, 1999). In that contribution, two mechanisms were identified to laterally move the COM towards the new travel direction (i.e. towards the center of the curve): foot placement and hip strategy.

Foot placement impacts the distance between the COM and the center of pressure (COP), and so alters the COM acceleration magnitude and direction (Winter, 1995). Therefore, when turning indications are provided in advance, lateral COM control during turning is initiated by placing the inner foot (i.e. the foot inner to the curved motion) closer to the outer one (i.e. the other foot), thus accelerating the lateral COM towards the center of curve (Patla et al, 1999).

In (Van der Noot et al, 2018), foot placement was mainly controlled during the supporting phase (i.e. stance phase excluding the last double support phase) of the contralateral leg, through the hip abductors (HAB) and adductors (HAD) muscles, in the lateral plane (see Fig. 1d). More precisely, a hip lateral reference angle $\varphi_{h,l,ref}$ was computed, based on a feedback controller constraining the lateral COM position around its reference $\Lambda^*_{ref,h}$. This is detailed in Appendix 7.1.

During straight walking, $\Lambda^*_{ref,h}$ was set to a fixed value $\Lambda_{ref,h}$. Steering motions require to augment this reference as $\Lambda^*_{ref,h,\{R,L\}} = \Lambda_{ref,h,\{R,L\}}\,(1+\Delta_\Lambda\,\Gamma_{\{R,L\}})$, where R,L stand for right or left leg and Δ_Λ is a scaling parameter. This moves the lateral COM position reference of the inner foot away from the outer foot during curved motion. As a consequence, the inner foot will come closer to the outer foot (see (Van der Noot et al, 2018) for more details about lateral control).

The other lateral COM strategy relies on controlling the body pendulum in the stance phase. This is achieved through the so-called hip strategy using muscle actuation at the hip and torso (Horak and Nashner, 1986). In fact, the body is controlled as a double pendulum with the lower limbs and the upper body moving in opposite directions, so that the COM moves towards the center of the curve (Patla et al, 1999).

In (Van der Noot et al, 2018), the lateral hip muscles received a first burst provided by neurons N_E (right leg) and N_F (left leg), acting at the beginning of the corresponding leg supporting phase. Then, a feedback controller was activated on the torso lateral lean angle to track a reference Ψ^*_{ref}. This is detailed in Appendix 7.1.

The hip strategy is mainly active during the outer leg stance phase, after completion of the foot placement strategy (Patla et al, 1999). In order to anticipate a possible change in steering direction with foot placement before activating the hip strategy, the values of the turning commands $\Gamma_{\{R,L\}}$ computed during the former gait cycle are used. More precisely, Γ_R^{-1} is equal to the value of Γ_R at the penultimate left strike, Γ_L^{-1} is equal to the value of Γ_L at the penultimate right strike.

First, the neuron N_E excitation (i.e. u_E) is augmented by a contribution equal to $\nu_l\,\Gamma_R^{-1}$, while u_F is augmented by $\nu_l\,\Gamma_L^{-1}$ (ν_l is a scaling parameter). This increases the CPG burst during curved motion and brings the torso closer to the hip, thus moving the COM towards the center of the curve. In order to achieve a similar effect for the feedback controller on the torso lateral lean angle, its reference is set as $\Psi^*_{ref,\{R,L\}} = \Psi_{ref}\,(1+\Delta_\Psi\,\Gamma^{-1}_{\{L,R\}})$, where Δ_Ψ is a scaling parameter.

3.2 Transverse hip control

The hip transverse joints control the foot orientation motion, and thus impact the biped change in heading. In (Courtine and Schieppati, 2003), six healthy male adults walked along straight and curved paths. When walking along a curved path, the body turning mainly occurred during the stance phase of the outer foot. It also appeared that the inner foot rotation occurred mostly during the inner limb swing phase.

In (Van der Noot et al, 2018), the transverse hip muscles (i.e. hip external (HER) and internal (HIR) rotator muscle groups, see Fig. 1) were controlled to maintain the corresponding joint in its homing position, as depicted in Fig. 1e. To do so, these two antagonist muscles received stimulations proportional to the output of a feedback controller on the hip transverse reference angle $\varphi_{h,t,ref}$ (set to zero for straight walking). This is detailed in Appendix 7.1.

To generalize this for curved motion, the $\varphi_{h,t,ref}$ reference angle must be adapted to produce leg transverse motion coherent with the observations of (Courtine and Schieppati, 2003). Therefore, the turning motion is expected to start approximately at the swing phase initiation of the inner foot, while the legs realignment (i.e. feet realigned with the waist in the transverse plane) is expected at the beginning of the swing phase of the outer foot. To keep things simple, the two legs transverse rotations are commanded simultaneously (i.e. turning and realignment of both legs happen at the same time).

Phase locking is thus crucial to synchronize legs rotation during the gait cycle. This mechanism is provided by the RG

neurons. N_1 and N_2 start firing respectively after the right and the left feet strikes. N_3 and N_4 fire during the rest of the gait, i.e. before the next strike happens (mainly during left swing phase for N_3 and right swing phase for N_4). This behavior can be observed in Fig. 4.

To achieve the requested synchronization, two new neurons are introduced: the "turning" neurons (TR), depicted in Fig. 2c. N_λ is expected to control left turning, while N_ξ is in charge of right turning. Taking inspiration from the Matsuoka rules detailed in Eq. (1), the $\eta_k [x_l]^+$ terms are recruited (introducing two gains η_n and η_o) to generate both excitation and inhibition of the TR neurons. N_λ is excited by N_3 to start leg rotation during the left leg swing motion, while N_ξ is excited by N_4, for symmetrical reasons. The legs realignment is achieved with inhibition connections, triggered during the outer leg swing phase. This is done with neuron N_4 for N_λ and N_3 for N_ξ. Their time derivative rules are thus the following:

$$\begin{aligned} \dot{x}_\lambda &= \frac{1}{\tau}(\eta_o [x_3]^+ - \eta_n [x_4]^+ [x_\lambda]^+_{1/0}) \\ \dot{x}_\xi &= \frac{1}{\tau}(\eta_o [x_4]^+ - \eta_n [x_3]^+ [x_\xi]^+_{1/0}) \end{aligned} \tag{2}$$

The $[\bullet]^+_{1/0}$ function returns 1 if its argument is positive, 0 otherwise. Its purpose is to prevent the corresponding neuron firing rate to become negative. The CPG network is incremented by these two (non-Matsuoka) TR neurons in Fig. 3. The firing rates evolution of N_λ and N_ξ are also displayed in Fig. 4.

Using these two new neurons, the hip transverse reference $\varphi_{h,t,ref}$ is computed as follows:

$$\begin{aligned} \varphi_{h,t,ref,R} &= -\Gamma_R^{-1} k_{y,in} [x_\xi]^+ - \Gamma_L^{-1} k_{y,out} [x_\lambda]^+ \\ \varphi_{h,t,ref,L} &= \Gamma_L^{-1} k_{y,in} [x_\lambda]^+ + \Gamma_R^{-1} k_{y,out} [x_\xi]^+ \end{aligned} \tag{3}$$

$k_{y,in}$ and $k_{y,out}$ are respectively scaling factors for the inner and outer legs. Similarly to the hip strategy (see Section 3.1), $\Gamma^{-1}_{\{R,L\}}$ is used instead of $\Gamma_{\{R,L\}}$, in order to engage heading modulation after the foot placement strategy.

3.3 Steering parameters optimization

Seven key turning parameters were introduced in Sections 3.1 and 3.2, namely $k_{y,in}$, $k_{y,out}$, Δ_Λ, Δ_Ψ, η_n, η_o and ν_l. While it is possible to manually tune them to achieve robust curved motion, another solution is to rely on an optimizer to find these parameters, while maximizing a desired fitness function.

In (Van der Noot et al, 2018), a set of optimized parameters achieving straight walking (called *reference controller*) was used in order to produce most results. Starting from this reference controller, a particle swarm optimization (PSO) algorithm (Kennedy and Eberhart, 1995) is run on the seven key turning parameters. The purpose is to achieve turning motion with the shortest steering radii (i.e. sharpest turns) without falling.

Therefore, the following scenario is used. The biped must walk during $90\,s$ with a fixed speed reference v_{ref} (see (Van der Noot et al, 2018)) and a changing heading reference h_{ref}. During the $[10;25]\,s$ time interval, h_{ref} is set to 0.3, during the $[30;45]\,s$ time interval to -0.6, during the $[50;65]\,s$ time interval to 0.9 and during the $[70;85]\,s$ time interval to -1.2. The rest of the time, h_{ref} is set to zero. Using this, the walker faces increasing heading references, in both directions. We arbitrarily chose to restrict the range of h_{ref} to $[-1;1]$ during on-line control, and to $[-1.2;1.2]$ during optimizations, so that the walker is optimized in tougher conditions, thus increasing its robustness for extreme heading references.

The resulting fitness function to be maximized is the cumulative increments in the heading angle (i.e. absolute walker direction angle measured in the transverse plane) during the time periods when h_{ref} is non zero.

4 Steering parameters evolution with speed

Seven key turning parameters were identified in Section 3. This section studies how these parameters adapt with forward speed, providing a single controller with optimal turning control for the whole range of speed commands.

4.1 Polynomial approximations

The evolution of the seven key turning parameters is performed as follows. For the whole range of speed references v_{ref} (i.e. from $0.4\,m/s$ to $0.9\,m/s$, with a discretization of $0.05\,m/s$), ten optimizations are performed for each target speed, according to the method introduced in Section 3.3. The corresponding results are reported in Fig. 5.

Intuitively, the evolution of these parameters can be approximated with polynomial functions. To select the appropriate orders capturing parameters evolution without overfitting, a model goodness-of-fit analysis using the sum of squared values of the prediction errors is used (Smith and Rose, 1995). In fact, for each polynomial order, the corresponding p-value is computed to measure the likeliness that the selected order is appropriate to represent the parameter evolution. More information is provided in (Van der Noot et al, 2018).

Table 1 reports the p-values corresponding to polynomial approximations of orders 0, 1 and 2 of the data provided in Fig. 5, based on the least square errors. Similarly to (Van der Noot et al, 2018), the first order with a p-value larger than 0.1 is selected (grey cells). This is a less strong

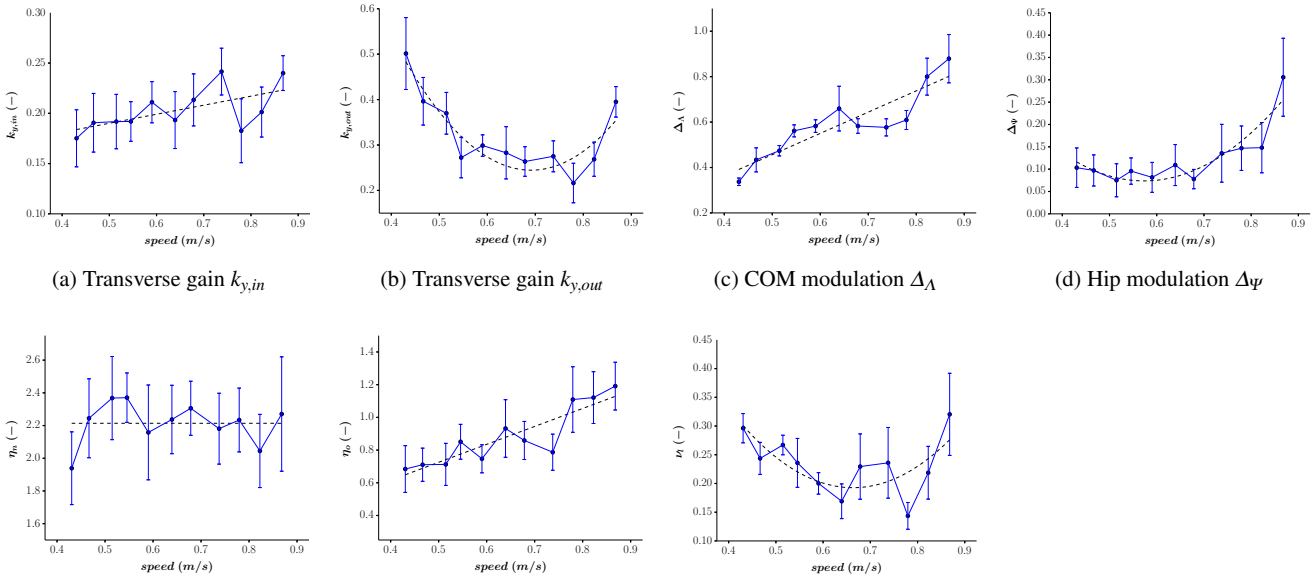

(a) Transverse gain $k_{y,in}$ (b) Transverse gain $k_{y,out}$ (c) COM modulation Δ_Λ (d) Hip modulation Δ_Ψ

(e) CPG connexion η_n (f) CPG connexion η_o (g) Lateral excitation ν_l

Fig. 5 Ten optimizations are performed for each target speed (from 0.4 m/s to 0.9 m/s with an interval of 0.05 m/s).The actual speed of each solution is measured (during straight walking), along with the optimized value of the seven key turning parameters. For each target speed, we gather the ten optimization final results, reporting their mean and standard deviations. For graph legibility, the error bars represent half of the standard deviations. Dashed lines correspond to the polynomial approximations whose order is reported in Table 1, using the minimum mean square error method.

analysis than rejecting the opposite null hypothesis, but is considered to be sufficient to design the control rules.

Table 1 Polynomial approximations: p-values

	order 0	order 1	order 2	selected
$k_{y,in}$	0.108	**0.342**	0.268	1
$k_{y,out}$	0	0	**0.163**	2
Δ_Λ	0	**0.001**	0.001	1
Δ_Ψ	0	0.028	**0.528**	2
η_n	**0.729**	0.645	0.691	0
η_o	0	**0.487**	0.54	1
ν_l	0.001	0.001	**0.044**	2

It appears from the results of Table 1 that two parameters (Δ_Λ and ν_l) did not reach the threshold of 0.1. For these two parameters, the order with the largest p-value was selected, i.e. 1 for Δ_Λ and 2 for ν_l. The $k_{y,in}$ p-value for order 0 barely exceeds the critical threshold of 0.1, while order 1 is much larger (i.e. close to 0.35). Therefore, we arbitrarily decided to select order 1 for this parameter. Regarding the η_n parameter, a polynomial approximation of order 0 was selected (i.e. constant value), thus reducing to six the number of key turning parameters evolving with speed. The polynomial approximations using the selected orders are depicted with dashed lines in Fig. 5.

4.2 Parameters analysis

The scaling parameters $k_{y,in}$ and $k_{y,out}$ are directly related to the curvature radius. Indeed, they control the legs transverse rotations, and so the turning. The inner foot parameter ($k_{y,in}$) increases with forward speed, favoring sharp turns for the highest speeds. The range of values obtained for the outer foot parameter ($k_{y,out}$) is larger than the one obtained for the inner foot ($k_{y,in}$). Therefore, $k_{y,out}$ appears to be more speed dependent than $k_{y,in}$. Here, the sharpest turns are obtained at speed extrema. Globally, the highest speed are expected to produce the largest curvatures. Indeed, despite their lower $k_{y,out}$ when compared to the slowest speeds, they also benefit from the largest $k_{y,in}$ parameters. In contrast, speeds in the middle of the range are expected to generate the most gentle turns.

Directly related to these parameters, the CPG excitation and inhibition weights η_n and η_o also affect the legs transverse rotations. Only the excitation parameter (η_0) appears to evolve with speed, producing larger commands for faster speeds. This increases the speed of the hip motion, as well as the plateau reached at the end of this initial motion, thus increasing the heading change. The constant η_n value is much larger than η_o, resulting in a quick realignment of the feet with the waist during the outer leg swing motion.

In the lateral plane, the inner foot initiates turning by coming closer to the outer one. This foot position strategy is

amplified with a bigger Δ_Λ. Therefore, the linear increase of this parameter with forward speed indicates that the walker takes advantage of the inertia effects to induce bigger accelerations towards the center of the curve, when walking at high speeds.

Finally, the lateral hip strategy is controlled by the remaining parameters ν_l (CPG excitation) and $\Delta\psi$ (reflex). Similarly to $k_{y,out}$, the highest values are reached at the boundaries of the speed range (especially at high speeds). Increasing the hip strategy effects appears therefore to be correlated with sharper turns.

4.3 Parameters co-optimization

The controller design can now be further extended to co-optimize all key turning parameters in a single optimization, therefore recruiting the optimal turning parameters for the whole speed range, and not for a single speed. The seven key parameters studied in Section 4.1 are replaced by polynomial approximations, whose order is selected according to Fig. 5 and Table 1. Because η_n is actually of order 0, the corresponding parameter is left as a constant.

The corresponding rules are reported in Appendix 7.2. They involve sixteen parameters to optimize, whose bounds are indicated in Table 2. A last optimization was then performed with the reference controller from (Van der Noot et al, 2018), in order to optimize these turning parameters. The resulting controller, combining forward speed and turning modulation, keeps the name *reference controller*. This controller is available inside a simulation code, provided as supplementary downloadable material (Online Resource 1).

5 Results

The results presented in this section were obtained using the reference controller, introduced in Section 4.3. The evolution of the walking curvature with heading reference is first studied before characterizing the gait main features. Finally, some tele-operated steering scenarios are presented.

5.1 Curvature radius control

The biped can achieve sharper turns when increasing its heading reference h_{ref}. However, this also depends on its walking speed (and so, on v_{ref}). This effect was first studied with the reference controller receiving three representative speed references: the middle of the speed range (i.e. $v_{ref} = 0.65\,m/s$) and two speeds close to the speed extrema ($0.45\,m/s$ and $0.85\,m/s$). To quantify it, the following experiment was performed. For each of the speed references, the biped received a heading reference ranging between 0 (i.e. straight walking) and 1 (i.e. maximal right steering command). The steady-state behavior thus corresponded to a motion being close to a circle (except for $h_{ref} = 0$): both speed and heading references were stationary and non-zero. The resulting curvature was measured as the inverse of the radius of the circle described by COMAN in steady-state, after a full rotation. Corresponding results are presented in Fig. 6. Because of the left/right symmetry, left steering is not reported.

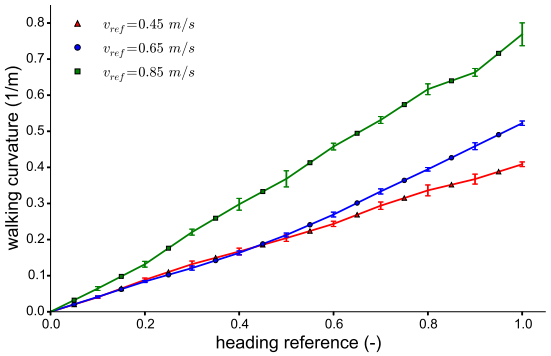

Fig. 6 For each representative speed references (i.e. v_{ref} set to $0.45\,m/s$, $0.65\,m/s$ or $0.85\,m/s$), COMAN received right heading references h_{ref} (from 0 to 1 with a discretization of 0.1). The walking curvature was measured from the circle described by the robot, over ten trials. The corresponding mean and standard deviations are reported. For left heading references (i.e. $h_{ref} < 0$), similar results were obtained (due to the symmetry of the configuration).

As expected, the curvature increased (sharper turns) with increasing h_{ref} commands. Moreover, a linear relationship was observed between the heading reference h_{ref} and the resulting curvature. This was mainly due to the transverse hip joints control, tracking position references proportional to h_{ref}. The curvature also depended on the speed reference v_{ref}. For large heading references, larger curvatures were obtained for faster speeds. However, this trend was not clear at lower speeds. Therefore, the experiment of Fig. 6 was extended to the whole range of speed references (i.e. from $0.4\,m/s$ to $0.9\,m/s$). Corresponding results are depicted in Fig. 7.

It appears that the curvatures ranged between 0 (i.e. straight walking, obtained with $h_{ref} = 0$) and 0.79 for these commands. As mentioned in Section 4.2, the sharpest turns were obtained for the fastest speeds (followed by the slowest ones for small h_{ref} commands), while the speeds around $0.55\,m/s$ provided the most gentle curves. This is mainly due to the large high-level parameters $k_{y,in}$ and $k_{y,out}$ which were obtained during the optimization process for the speed extrema (see Section 4.2).

Importantly, collisions between legs were frequently observed for heading references h_{ref} larger or equal to 0.5. These collisions could also be sometimes detected for lower h_{ref} values, especially for speed references close to the ex-

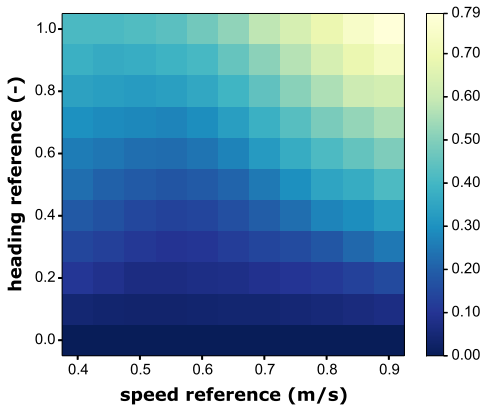

Fig. 7 Similarly to Fig. 6, the walking curvature was measured when COMAN received right heading references. This is presented here for the whole spectrum of speed references, i.e. from $0.4\,m/s$ to $0.9\,m/s$, with a discretization of $0.05\ m/s$. The color map represents the resulting walking curvature (in m^{-1}, averaged over ten runs).

trema. In fact, this problem was already observed in (Van der Noot et al, 2018) for straight walking at speed extrema. This issue is further discussed in Section 6.4.

5.2 Gait main features evolution with turning reference

The following gait features were studied: speed, stride length, stride period and swing ratio. Their evolution with h_{ref} (positive for right turns) is reported in Fig. 8 for the same three representative speed references used in Section 5.1 (i.e. $0.45\,m/s$, $0.65\,m/s$ and $0.85\,m/s$).

Regarding speed evolution, Fig. 8a shows that the speed remained quite constant and close to its reference when this reference v_{ref} was set to $0.65\,m/s$. In contrast, the other v_{ref} values resulted in speeds converging towards the middle of the speed range. Both in (Courtine et al, 2006) and (Courtine and Schieppati, 2003), human subjects tended to steadily decrease their speed when facing an increasing curvature. During these two experiments, the mean velocity of the subject was around $68\%\,BH/s$, where BH stands for body height. Considering that COMAN height would be close to $1.06\,m$ if it had a head, this corresponds to a speed of $0.72\,m/s$, so in between $0.65\,m/s$ and $0.85\,m/s$. Therefore, our results reporting a speed decrease are consistent with human observations.

When comparing the stride length (Fig. 8b) and the stride period (Fig. 8c), it clearly appears that the change in speed was mainly correlated with the stride length evolution. During curved trajectories, the stride lengths of the inner and outer limbs were expected to differ, in contrast to straight walking. Indeed, the external leg covered a longer path because its foot moved along a circular trajectory whose radius was larger than the one of the inner foot (Courtine and Schieppati, 2003). This is consistent with the results of Fig. 8b where the inner (right) stride length became significantly lower than the outer (left) one, as the turning reference increased. In (Courtine et al, 2006), it was observed that the stride length modification during turning (compared to straight walking) mainly affected the inner limb. In Fig. 8b, this trend is not observed: both the inner and outer legs stride lengths were affected. This is potentially related to the transverse hip control rules being recruited (see Section 3.2).

The stride period evolution with turning reference in Fig. 8c is not significant. A small increase was observed for the highest heading references when v_{ref} was set to $0.45\,m/s$ or $0.65\,m/s$, while the highest speed reference ($0.85\,m/s$) oscillated around its mean value with higher standard deviations. Similarly, (Courtine et al, 2006) observed that human gait cycle duration was hardly affected by the curvature of the path. Only the tighter curves caused a modest increase in cycle duration.

Results of Fig. 8c could not be decomposed between right and left contributions because the averaged stride period had to be the same for both legs. However, the portion of time when each leg was in swing phase (over the whole gait cycle) was leg-dependent, as presented in Fig. 8d.

In (Courtine et al, 2006), both legs exhibited similar stance durations during straight-walking but showed opposite modulation of stance duration during curved motion. A similar behavior can be seen in Fig. 8d, especially, for v_{ref} set to $0.45\,m/s$ or $0.65\,m/s$. However, (Courtine et al, 2006) also observed that the swing duration of the inner leg significantly decreased with curvature, while changes in stance duration of the outer limb were less pronounced. Only the speed reference of $0.85\,m/s$ (with h_{ref} smaller than 0.7) showed a lower swing ratio for the inner limb, compared to the outer one. The swing ratio evolution in Fig. 8c being relatively small, this result is less significant, but still indicates some discrepancy compared to human walking.

5.3 Robustness when turning

In order to compare the robustness of the controller during straight and curved walking, the following experiment was performed. COMAN received random pushes on the torso when walking at different speeds. First, these pushes were applied during straight walking with a magnitude selected between $0\,N$ and $25\,N$, during $0.2\,s$ in the transverse plane. These pushes were applied with a time interval randomly selected between 5 and $6\,s$. Each push orientation in the transverse plane was randomly selected in the $]-\pi;\pi]$ interval (i.e. all possible directions with an equal probability). The torque noise presented in Section 2.3 was active. The robot was blind, i.e. it had no other feedback than the reflexes driving its neural controller.

Robustness was quantified by measuring the time the robot could walk without falling, when facing these pushes.

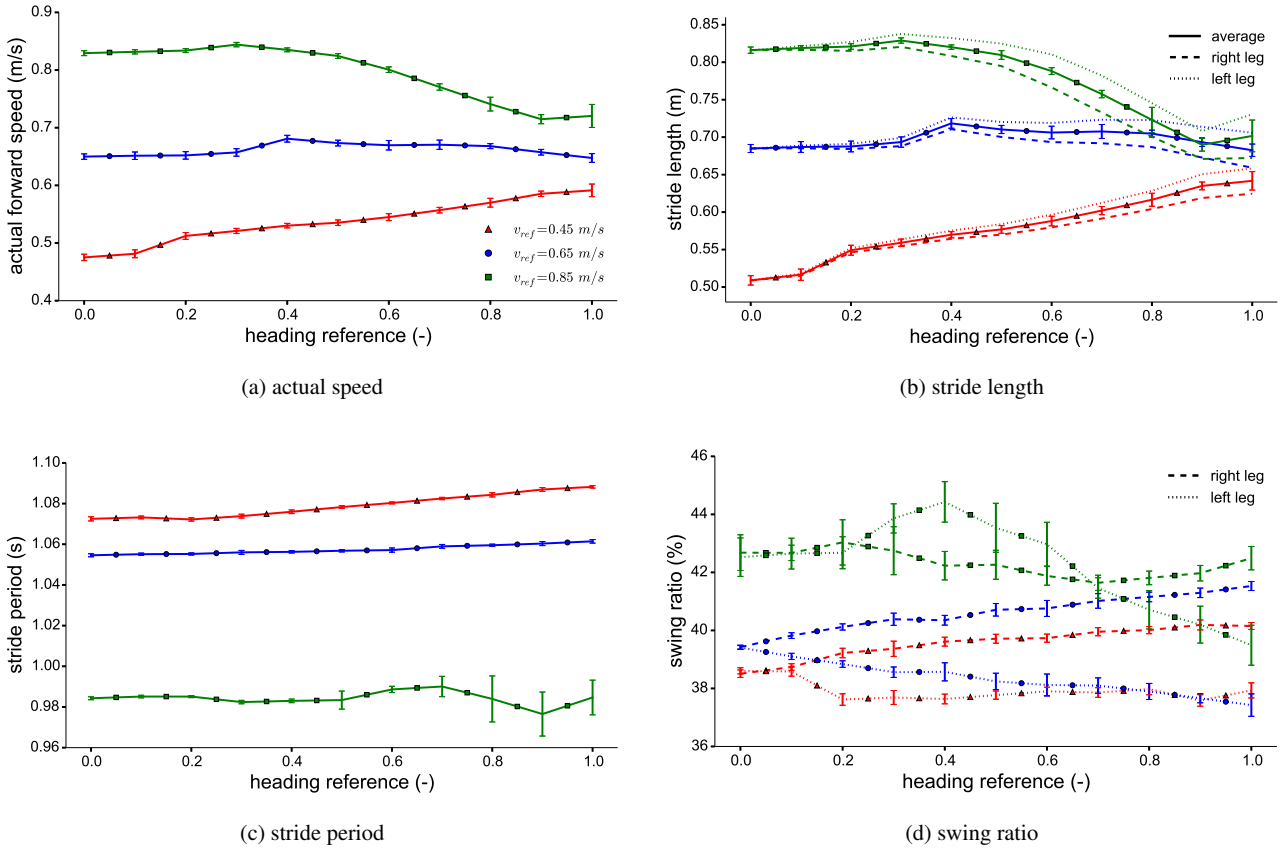

(a) actual speed

(b) stride length

(c) stride period

(d) swing ratio

Fig. 8 The evolution of some gait features with the heading reference h_{ref} is studied, while the reference controller receives three distinct speed references v_{ref}: $0.45\,m/s$ (triangles), $0.65\,m/s$ (circles) and $0.85\,m/s$ (squares), same legend in the four panels. Panel (a) presents the actual walker speed. In panel (b), the average stride length (solid) is decomposed between right (dashed) and left (dotted) leg contributions. Panel (c) shows the evolution of the stride period. Finally, the ratio of time during which each leg is in swing phase is presented in panel (d). For each measurement, ten simulation runs were performed. Their mean and standard deviations are displayed. For graph legibility, panel (b) only depicts the standard deviation of the average stride length (standard deviations of each leg are similar to this average value). These results are presented during right steering experiments, but are similar for left turns, due to the symmetry of the configuration.

The time count started during steady-state walking, when the external pushes started, and was limited to an upper bound of $50\,s$. The results are reported in Fig. 9a.

Globally, faster speeds could resist to larger pushes. The only exception was the maximal speed reference ($v_{ref} = 0.9\,m/s$), which was less stable. Indeed, less robust gaits were usually obtained for the extrema of the optimized speed range.

The same experiment was performed during turning motion, when receiving right heading references h_{ref} ranging between 0 and 1, through steps of 0.1. This was tested for the following set of push amplitudes: $0\,N$ (Fig. 9b), $5\,N$ (Fig. 9c), $10\,N$ (Fig. 9d), $15\,N$ (Fig. 9e) and $20\,N$ (Fig. 9f).

Globally, the walker robustness was not significantly deteriorated with increasing turning references, with one notable exception: the highest speeds v_{ref} with the highest heading references h_{ref}, usually causing a quick fall of the walker. In particular, this was also observed without external pushes (i.e. only with torque noise reading), as depicted in Fig. 9b. However, this corresponds to very small steering radii, up to $1.26\,m$ (i.e. corresponding to curvatures up to 0.79, see Fig. 7). This smallest radius is about twice the size of the robot leg, and thus represents a very sharp turn for COMAN.

Interestingly, for speed references up to $0.65\,m/s$, the walker barely never fell when receiving pushes up to $5\,N$, even for extreme h_{ref} commands. For higher push amplitudes, a slight decrease in robustness was observed with higher h_{ref}. However, this usually corresponds to push amplitudes also causing falls in straight walking gaits (see Figs. 9e and 9f).

5.4 Tele-operated steering

Using the reference controller, it is possible for a human tele-operator to achieve on-line control of both speed and steering (direction and curvature). In particular, this can be done using a single joystick, e.g. with one axis controlling

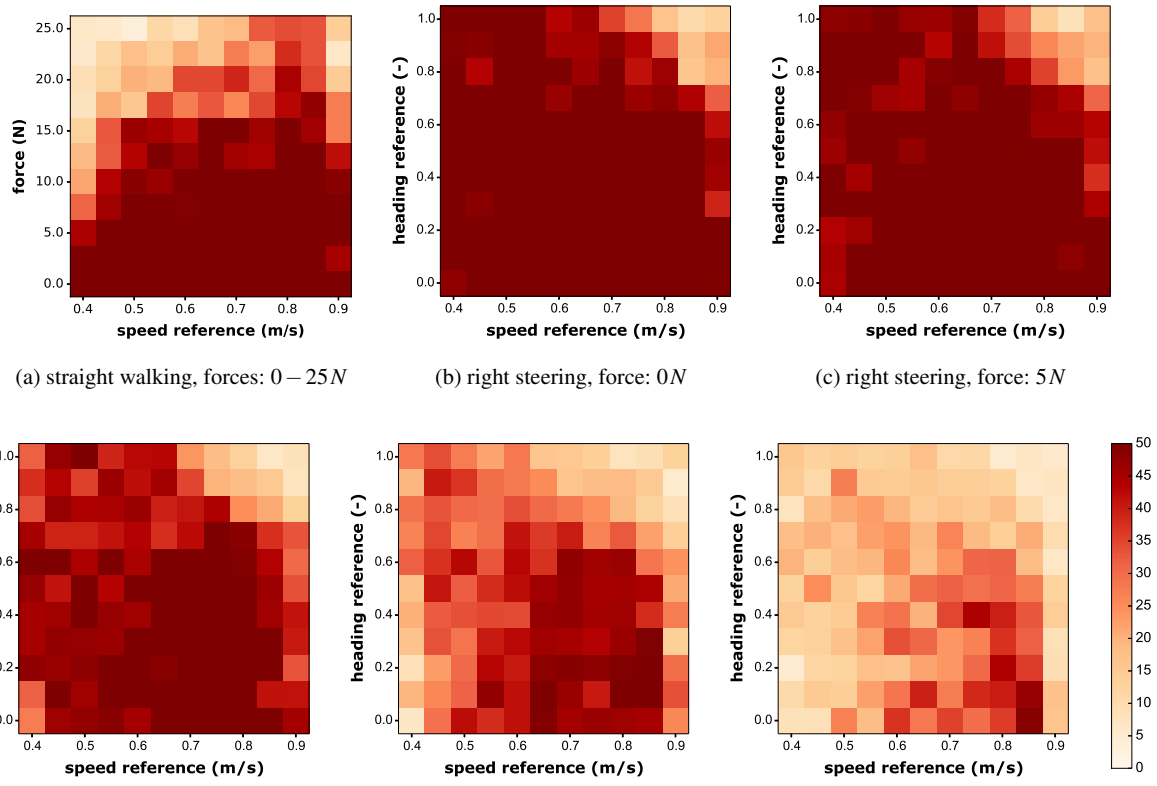

(a) straight walking, forces: $0-25N$ (b) right steering, force: $0N$ (c) right steering, force: $5N$

(d) right steering, force: $10N$ (e) right steering, force: $15N$ (f) right steering, force: $20N$

Fig. 9 For the whole spectrum of speed references, pushes were applied to the torso of COMAN, as described in Section 5.3. The color map represents the time the robot could walk before falling (in [s], averaged over ten runs and limited to $50s$). In panel (a), different push amplitudes were selected during straight walking. In the other panels, a single push amplitude was selected ($0N$ (b), $5N$ (c), $10N$ (d), $15N$ (e) or $20N$ (f)) while the biped received increasing right heading references h_{ref}. These graphs are similar for left steering, due to the left/right symmetry.

v_{ref} in the $[0.4;0.9]m/s$ range and the other axis controlling h_{ref} in the $[-1;1]$ range. This allows an intuitive control and modulation of the robot gait, which can be used to freely navigate in a cluttered environment. Snapshots of such a modulation are visible in Fig. 10.

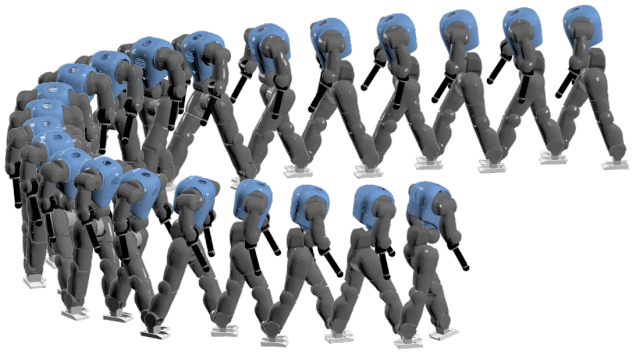

Fig. 10 Receiving a speed reference v_{ref} of 0.65 m/s, the robot walks with an initial heading reference h_{ref} of 0 (straight walking) before changing this command to -1 (maximum left steering).

A longer walk experiment is visible in the Online Resource 2 (video provided as supplemental material). During that experiment, COMAN received speed and heading references whose evolution with time is depicted in Fig. 11. The trajectory of COMAN during this last experiment is visible in Fig. 12, where its footprints are depicted together with the evolution of its COM and center of pressure (COP). Steering was performed in both directions, and with different curvatures.

Finally, this deliberate steering can also be used to avoid stepping into holes, as presented in the Online Resource 3 (video provided as supplemental material). In that last experiment, different commands were sent to the walker before stepping into different holes. According to the command received, the biped either fell or succeeded to avoid the hole. In (Van der Noot et al, 2015b), we presented a similar experiment for a 2D scenario (i.e. with the biped waist artificially constrained to stay in the sagittal plane) where the modulation of v_{ref} resulted in a successful crossing of a hole.

6 Discussion

In this contribution, we presented a 3D walking controller that can generate human-like walking gaits and can modulate its walking speed and heading direction. By embracing the concept of the limit cycle, it relaxes constraints inherent to more traditional walker controllers, therefore achieving faster, more energetically efficient and more human-like (e.g. straight knee walking) gaits. However, the walker still features on-line adaptation capabilities. On top of its forward speed modulation, the biped is capable of controlling its steering direction and curvature. The resulting walking controller is therefore capable of fully navigating in a cluttered environment (with a nearly-flat ground), by avoiding obstacles.

6.1 Gait modulation

The whole controller, combining CPG and reflexes, can be obtained by two successive optimizations. In the first one, straight walking control is obtained as described in (Van der Noot et al, 2018), while the second optimization provides turning capabilities. These two optimizations are performed on the whole speed range (i.e. from 0.4 to $0.9 m/s$), therefore co-optimizing all the parameters, in order to increase the performances (energy efficiency, robustness, speed modulation, turning control) for any achievable speed.

Speed and curved motions can then be controlled by modulating the speed reference v_{ref} and the heading reference h_{ref} inputs, thus providing high-level inputs for on-line control. In sum, we managed to combine the benefits of limit cycle walkers with the capacity to steer the robot velocity and direction.

This control framework is coherent with the observations of (Arechavaleta et al, 2008). In their experiments, human subjects were allowed to choose their natural walking speed and trajectory to reach several target points with different orientations. They observed that human locomotion obeys a nonholonomic system with linear and angular velocity as inputs.

In the literature, similar skills were usually achieved using inverse kinematics/dynamics methods relying on optimization-based controllers, like whole-body control. Therefore, these approaches can treat turning in the context of a global optimization problem. For instance, (Faraji et al, 2014) used a model predictive control to plan optimal future footsteps, given desired sagittal and steering velocities. These footsteps were later mapped to desired accelerations, in turn converted to joint torques through an appropriate whole-body optimization layer. Similarly, (Deits and Tedrake, 2014) developed an optimization-based method for planning footstep placements, while handling obstacles avoidance and kinematic reachability.

In sum, these methods offered a mathematical framework to incorporate steering commands in a whole optimization process. However, as emphasized in the introduction, they have their own flaws like energy inefficiency, unnatural gait and slow walking speeds. Our previous contribution (Van der Noot et al, 2018) showed that bio-inspired approaches can solve these problems. By incrementing it with steering capabilities, our framework thus offers to handily tele-operate the biped with few commands, while exhibiting human-like gait features.

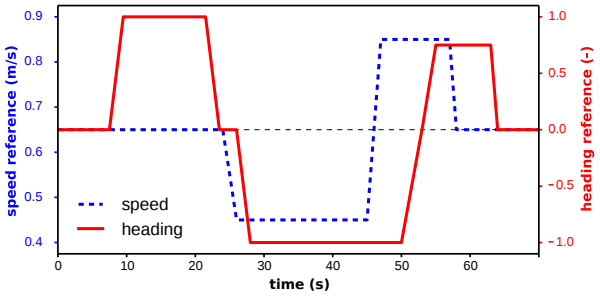

Fig. 11 Temporal evolution of the commands used during the walk experiment recorded in the animation (Online Resource 2) and depicted in Fig. 12. More precisely, the speed reference v_{ref} and the heading reference h_{ref} control respectively the biped forward speed and its curved motion.

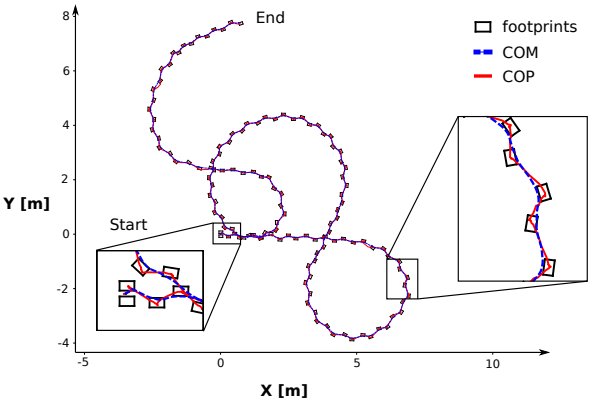

Fig. 12 Footprints of COMAN on a planar ground, when walking while being tele-operated by a human. This corresponds to the experiment recorded in the animation (Online Resource 2), with the commands depicted in Fig. 11. The evolution of the center of mass projected on the ground (COM) and of the center of pressure (COP) are also depicted.

6.2 Walker robustness

Humanoid robots are currently far from reaching the impressive robustness of real humans during locomotion. This is

one of the main reasons preventing them from being used outside controlled environments like laboratories. In the blind walking experiments of Section 5.3, our robot could naturally resist to pushes, both for straight walking and during curved motion. Interestingly, this was achieved without changing a single parameter of the controller. This is potentially related to the viscoelastic muscle properties, inducing gait adaptations to perturbed environments. However, the effects of these viscoelastic properties regarding the walking robustness remains to be quantified.

Importantly, additional strategies should probably be implemented to sustain stronger pushes. For instance, (Heremans et al, 2016) developed a neural controller progressively learning appropriate muscular stimulations to reject disturbances. Because this approach also relies on a musculo-skeletal model, it is compatible with the controller presented in this paper.

Robustness can also be improved by using a more bio-inspired embodiment. For instance, the rigid foot used here is very different from the flexible human one. In (Colasanto et al, 2015), we showed that replacing the robot rigid foot by a model of a human prosthesis led to more robust gaits. Indeed, in contrast to many approaches requiring to keep the feet flat on the ground, this constraint is not inherent to our bio-inspired approach.

6.3 Human steering strategies

While the recruitment of CPGs in locomotion control is widely accepted for many vertebrates, its involvement in human locomotion is still open to debate (Minassian et al, 2017). For instance, the work of (Geyer and Herr, 2010), further extended in (Song and Geyer, 2015), generated human-like gaits with speed modulation and steady turning motions, although they implemented only reflex pathways (i.e. without CPG).

Here, speed and heading modulations were achieved by controlling two reference inputs (v_{ref} and h_{ref}), resulting in linear or quadratic adaptations of fifteen key control parameters. The modulation of this small set of parameters resulted in drastic gait modulations. Indeed, the speed could be modulated in the $[0.4; 0.9]\,m/s$ range, as a result of both step length and frequency adaption; while the footstep landing positions and heading modulation could steer the walker in a 3D environment to follow a given path or to avoid obstacles.

Among this set of fifteen key control parameters, only four act on reflexes (the others being CPG-related). Therefore, while the recruitment of CPG networks during human locomotion remains a matter open to debate, our work showed that they play a significant role in reducing the complexity of gait modulation.

Regarding transverse hip joint angle, its motion was controlled to track a reference position reproducing observations of real human walking (Courtine et al, 2006; Courtine and Schieppati, 2003). Rather than a direct angle control, the controller could possibly be adapted by mixing the CPG turning outputs with new reflex signals. For instance, the contractile length l_{ce} of the HER and HIR muscles could be recruited to provide an indirect biological measurement of the hip transverse motion, similarly to the reflex driving the TA muscle (inspired from (Geyer and Herr, 2010)).

Other possible human strategies could drive the refinement of the proposed controller. For example, humans also move the hip internal rotation during straight walking. This moves the swing leg forward and thus increases the step length (Stokes et al, 1989). This observation could be used to achieve similar leg transverse motion during straight walking. During turning motions, the transverse hip control rules could also be adapted to mainly affect the stride length of the inner limb, as mentioned in Section 5.2.

6.4 Perspectives

The controller developed in this contribution can be used in various domains, like robotics, neuroscience (investigating human locomotion), and 3D animation, in order to generate physically plausible gaits with speed and turning control (Wang et al, 2012; Geijtenbeek et al, 2013).

Currently, the biped can be steered by a human operator to navigate in a cluttered environment, while avoiding obstacles like holes (see Section 5.4). Additional controllers could be developed to automatically command the robot. For instance, a higher-level layer could be in charge of finding the (v_{ref}, h_{ref}) commands to reach desired footstep locations.

The controller robustness can also be improved for sharp turns, by developing new stabilization strategies. The reachable curvatures could be extended, but this is less relevant. Indeed, the controller is already capable of reaching steering radii which are approximately twice the size of the walker leg length. Below this limit, curved motion becomes unnatural and could possibly be replaced by side-stepping strategies.

As pointed in Section 5.1, the hip lateral position could sometimes bring the swing leg too close to the stance one, possibly causing collisions between both. In our experiments, this could mainly happen for extreme speed, high heading references, or during perturbed walking. A first solution would be to adapt the optimization fitness (see Section 3.3) by rewarding solutions without collision. However, this issue is more related to the optimization of the straight walking, as discussed in (Van der Noot et al, 2018). As pointed in that contribution, a future perspective would be to increment the lateral hip control during swing phase to avoid collisions.

Importantly, this might also change as a function of the walker embodiment being used.

Last but not least, the controller developed here could be tested with a real robotic device. Indeed, all the experiments in this contribution were performed using a faithful simulation model of the COMAN platform (including its actuator dynamics and noisy torque sensing). Despite the huge gap between human walking capabilities and humanoid robot ones, this contribution illustrates that bio-inspiration can help to progressively bridge this gap.

7 Appendices

7.1 Appendix 1 - Stimulations for curved motion

The stimulations computation rules from (Van der Noot et al, 2018) affected by the curved motion updates (see Section 3) are summarized here. More details (e.g. time delays) are provided in that former contribution. Variables presented in Section 3 are not detailed here.

The hip lateral joints are controlled by the HAB and HAD muscles. First, the HAB muscles receive stimulations coming from the CPG. These stimulations are mainly proportional to $[x_E]^+$ (excited by u_E) for the right leg and to $[x_F]^+$ (excited by u_F) for the left leg.

During the leg supporting phase, the following proportional-derivative (PD) control is applied: $\Delta_{\Psi,\{R,L\}} = (k_{p,\Psi}\,(\delta\,\Psi^*_{ref,\{R,L\}} - \Psi_t) - k_{d,\Psi}\,\dot{\Psi}_t)\,\tilde{F}_{gd,\{R,L\}}$, where $k_{p,\Psi}$ and $k_{d,\Psi}$ are parameters to optimize, Ψ_t is the torso lateral lean angle and $\dot{\Psi}_t$ is its derivative. δ equals 1 for the right leg and -1 for the left one. Finally, $\tilde{F}_{gd,\{R,L\}}$ is the vertical force below the corresponding foot, normalized to the walker weight. Then, HAB and HAD muscles are mainly commanded by a stimulation equal to $[\Delta_{\Psi,\{R,L\}}]^+$ or $[\Delta_{\Psi,\{R,L\}}]^-$.

During the contralateral leg supporting phase, a hip lateral reference angle $\varphi_{h,l,ref,\{R,L\}}$ is computed as $-k_{p,\Lambda,h}$ $(-\delta\,\Lambda^*_{ref,h,\{R,L\}} - \Delta_{com,\{L,R\}}) + k_{d,\Lambda,h}\,\dot{\Delta}_{com,\{L,R\}}$, where $k_{p,\Lambda,h}$ and $k_{d,\Lambda,h}$ are control parameters to optimize, $\Delta_{com,L}$ is the COM lateral position, relative to the left foot and $\dot{\Delta}_{com,L}$ its derivative (similar for $\Delta_{com,R}$ and $\dot{\Delta}_{com,R}$ relative to the right foot). The resulting local angle reference $\varphi_{h,l,ref,\{R,L\}}$ is later maintained by using a similar PD control rule as described above (i.e. for the supporting phase), with similar stimulations sent to HAB and HAD.

The hip transverse joints are controlled with the following PD computation: $\Delta_{trans,\{R,L\}} = 500\,(\varphi_{h,t,ref,\{R,L\}} - \varphi_{h,t,\{R,L\}}) - 20\,\dot{\varphi}_{h,t,\{R,L\}})$, where $\varphi_{h,t,\{R,L\}}$ is the hip joint transverse position and $\dot{\varphi}_{h,t,\{R,L\}}$ is its derivative. Stimulation equal to $[\Delta_{trans,\{R,L\}}]^+$ or $[\Delta_{trans,\{R,L\}}]^-$ are then sent to the HER and HIR muscles.

7.2 Appendix 2 - Optimization parameters

The parameters to be optimized in the controller, and their ranges are reported Table 2: the transverse (t) and lateral (l) leg parameters, as well as the CPG-related parameters. The speed dependent parameters are computed as follows: $k_{y,in} = K_{y,in} + L_{y,in}\,v_*$; $k_{y,out} = K_{y,out} + L_{y,out}\,v_* + M_{y,out}\,v_*^2$; $\Delta_\Lambda = K_{\Delta,\Lambda} + L_{\Delta,\Lambda}\,v_*$; $\Delta_\Psi = K_{\Delta,\Psi} + L_{\Delta,\Psi}\,v_* + M_{\Delta,\Psi}\,v_*^2$; $\eta_o = K_{\eta,o} + L_{\eta,o}\,v_*$; $\nu_l = K_{\nu,l} + L_{\nu,l}\,v_* + M_{\nu,l}\,v_*^2$, where $v_* = v_{ref} - 0.65$ and v_{ref} is the target forward speed. The parameters optimized for the reference controller are provided in the simulation code extension (Online Resource 1).

Table 2 Optimization parameters and their bounds

	min	max		min	max
leg (t)			**leg (l)**		
$K_{y,in}$	0.1	0.4	$K_{\Delta,\Lambda}$	0.2	1
$K_{y,out}$	0.1	0.5	$K_{\Delta,\Psi}$	0	0.3
$L_{y,in}$	0	0.4	$L_{\Delta,\Lambda}$	0	2
$L_{y,out}$	-0.6	0.2	$L_{\Delta,\Psi}$	-0.2	0.6
$M_{y,out}$	0	6	$M_{\Delta,\Psi}$	0	4
CPG (η)			**CPG (ν)**		
η_n	1.6	3.2	$K_{\nu,l}$	0.05	0.35
$K_{\eta,o}$	0.4	1.4	$L_{\nu,l}$	-0.15	0.15
$L_{\eta,o}$	0	2	$M_{\nu,l}$	0	4

References

Aoi S, Tsuchiya K (2005) Locomotion Control of a Biped Robot Using Nonlinear Oscillators. Autonomous Robots 19(3):219–232, DOI 10.1007/s10514-005-4051-1

Arechavaleta G, Laumond JP, Hicheur H, Berthoz A (2008) An Optimality Principle Governing Human Walking. IEEE Transactions on Robotics 24(1):5–14, DOI 10.1109/TRO.2008.915449

Chestnutt J, Lau M, Cheung G, Kuffner J, Hodgins J, Kanade T (2005) Footstep Planning for the Honda ASIMO Humanoid. In: Proceedings of the 2005 IEEE International Conference on Robotics and Automation, IEEE, pp 629–634, DOI 10.1109/ROBOT.2005.1570188

Colasanto L, Van der Noot N, Ijspeert AJ (2015) Bio-inspired walking for humanoid robots using feet with human-like compliance and neuromuscular control. In: 2015 IEEE-RAS 15th International Conference on Humanoid Robots (Humanoids), pp 26–32, DOI 10.1109/HUMANOIDS.2015.7363518

Collins S, Ruina A (2005) A Bipedal Walking Robot with Efficient and Human-Like Gait. In: Proceedings of the 2005 IEEE International Conference on Robotics and Automation, IEEE, pp 1983–1988, DOI 10.1109/ROBOT.2005.1570404

Courtine G, Schieppati M (2003) Human walking along a curved path. I. Body trajectory, segment orientation and the effect of vision. The European Journal of Neuroscience 18(1):177–190

Courtine G, Papaxanthis C, Schieppati M (2006) Coordinated modulation of locomotor muscle synergies constructs straight-ahead and curvilinear walking in humans. Experimental brain research 170(3):320–35, DOI 10.1007/s00221-005-0215-7

Daley MA, Felix G, Biewener AA (2007) Running stability is enhanced by a proximo-distal gradient in joint neuromechanical control. The Journal of experimental biology 210(Pt 3):383–394, DOI 10.1242/jeb.02668

Dallali H (2011) Modelling and dynamic stabilization of a compliant humanoid robot, CoMan. PhD thesis, University of Manchester

Dallali H, Mosadeghzad M, Medrano-Cerda Ga, Docquier N, Kormushev P, Tsagarakis N, Li Z, Caldwell D (2013) Development of a dynamic simulator for a compliant humanoid robot based on a symbolic multibody approach. In: 2013 IEEE International Conference on Mechatronics, ICM 2013, IEEE, pp 598–603, DOI 10.1109/ICMECH.2013.6519110

Deits R, Tedrake R (2014) Footstep planning on uneven terrain with mixed-integer convex optimization. In: 2014 IEEE-RAS International Conference on Humanoid Robots, pp 279–286, DOI 10.1109/HUMANOIDS.2014.7041373

Desai R, Geyer H (2013) Muscle-reflex control of robust swing leg placement. In: 2013 IEEE International Conference on Robotics and Automation, IEEE, pp 2169–2174, DOI 10.1109/ICRA.2013.6630868

Docquier N, Poncelet A, Fisette P (2013) ROBOTRAN: a powerful symbolic generator of multibody models. Mechanical Sciences 4(1):199–219, DOI 10.5194/ms-4-199-2013

Dzeladini F, van den Kieboom J, Ijspeert A (2014) The contribution of a central pattern generator in a reflex-based neuromuscular model. Frontiers in Human Neuroscience 8(June):1–18, DOI 10.3389/fnhum.2014.00371

Eilenberg MF, Geyer H, Herr H (2010) Control of a powered ankle-foot prosthesis based on a neuromuscular model. IEEE transactions on neural systems and rehabilitation engineering : a publication of the IEEE Engineering in Medicine and Biology Society 18(2):164–173, DOI 10.1109/TNSRE.2009.2039620

Faraji S, Pouya S, Ijspeert A (2014) Robust and Agile 3d Biped Walking With Steering Capability Using a Footstep Predictive Approach. Robotics: Science and Systems Foundation, DOI 10.15607/RSS.2014.X.028

Fitzpatrick P, Harada K, Kemp CC, Matsumoto Y, Yokoi K, Yoshida E (2016) Humanoids. In: Siciliano B, Khatib O (eds) Springer Handbook of Robotics, Springer International Publishing, pp 1789–1818

Geijtenbeek T, van de Panne M, van der Stappen AF (2013) Flexible Muscle-based Locomotion for Bipedal Creatures. ACM Trans Graph 32(6):206:1–206:11, DOI 10.1145/2508363.2508399

Geyer H, Herr H (2010) A muscle-reflex model that encodes principles of legged mechanics produces human walking dynamics and muscle activities. IEEE transactions on neural systems and rehabilitation engineering : a publication of the IEEE Engineering in Medicine and Biology Society 18(3):263–73, DOI 10.1109/TNSRE.2010.2047592

Heremans F, Van der Noot N, Ijspeert AJ, Ronsse R (2016) Bio-inspired balance controller for a humanoid robot. In: 2016 6th IEEE International Conference on Biomedical Robotics and Biomechatronics (BioRob), pp 441–448, DOI 10.1109/BIOROB.2016.7523667

Hill AV (1938) The Heat of Shortening and the Dynamic Constants of Muscle. Proceedings of the Royal Society B: Biological Sciences 126(843):136–195, DOI 10.1098/rspb.1938.0050

Hobbelen D, Boer Td, Wisse M (2008) System overview of bipedal robots Flame and TUlip: Tailor-made for Limit Cycle Walking. In: 2008 IEEE/RSJ International Conference on Intelligent Robots and Systems, pp 2486–2491, DOI 10.1109/IROS.2008.4650728

Hobbelen DGE, Wisse M (2007) Humanoid Robots, Human-like Machines - Chapter 14: Limit Cycle Walking DOI 10.5772/4808

Horak FB, Nashner LM (1986) Central programming of postural movements: adaptation to altered support-surface configurations. Journal of Neurophysiology 55(6):1369–1381

Ijspeert AJ (2008) Central pattern generators for locomotion control in animals and robots: A review. Neural Networks 21(4):642–653, DOI 10.1016/j.neunet.2008.03.014

Johnson M, Shrewsbury B, Bertrand S, Calvert D, Wu T, Duran D, Stephen D, Mertins N, Carff J, Rifenburgh W, Smith J, Schmidt-Wetekam C, Faconti D, Graber-Tilton A, Eyssette N, Meier T, Kalkov I, Craig T, Payton N, McCrory S, Wiedebach G, Layton B, Neuhaus P, Pratt J (2016) Team IHMC's Lessons Learned from the DARPA Robotics Challenge: Finding Data in the Rubble. Journal of Field Robotics DOI 10.1002/rob.21674

Kaneko K, Kanehiro F, Kajita S, Yokoyama K, Akachi K, Kawasaki T, Ota S, Isozumi T (2002) Design of prototype humanoid robotics platform for HRP. In: IEEE/RSJ International Conference on Intelligent Robots and System, IEEE, vol 3, pp 2431–2436, DOI 10.1109/IRDS.2002.1041632

Kennedy J, Eberhart R (1995) Particle swarm optimization. In: Proceedings of ICNN'95 - International Conference on Neural Networks, IEEE, vol 4, pp 1942–1948, DOI

10.1109/ICNN.1995.488968

Kuo AD (2002) The relative roles of feedforward and feedback in the control of rhythmic movements. Motor Control 6(2):129–145

Kurazume R, Tanaka S, Yamashita M, Hasegawa T, Yoneda K (2005) Straight legged walking of a biped robot. In: 2005 IEEE/RSJ International Conference on Intelligent Robots and Systems, IEEE, pp 337–343, DOI 10.1109/IROS.2005.1545447

Matsuoka K (1985) Sustained oscillations generated by mutually inhibiting neurons with adaptation. Biological cybernetics 52(6):367–376, DOI 10.1007/BF00449593

Matsuoka K (1987) Mechanisms of frequency and pattern control in the neural rhythm generators. Biological Cybernetics 56(5-6):345–353, DOI 10.1007/BF00319514

McCrea DA, Rybak IA (2008) Organization of mammalian locomotor rhythm and pattern generation. Brain Research Reviews 57(1):134–146, DOI 10.1016/j.brainresrev.2007.08.006

McGeer T (1990) Passive Dynamic Walking. The International Journal of Robotics Research 9(2):62–82, DOI 10.1177/027836499000900206

Minassian K, Hofstoetter US, Dzeladini F, Guertin PA, Ijspeert A (2017) The Human Central Pattern Generator for Locomotion: Does It Exist and Contribute to Walking? The Neuroscientist DOI 10.1177/1073858417699790

Patla AE, Adkin A, Ballard T (1999) Online steering: coordination and control of body center of mass, head and body reorientation. Experimental Brain Research 129(4):629–634, DOI 10.1007/s002210050932

Paul C, Bellotti M, Jezernik S, Curt A (2005) Development of a human neuro-musculo-skeletal model for investigation of spinal cord injury. Biol Cybern 93(3):153–170, DOI DOI10.1007/s00422-005-0559-x

Rossignol S, Dubuc R, Gossard JP (2006) Dynamic sensorimotor interactions in locomotion. Physiological reviews 86(1):89–154, DOI 10.1152/physrev.00028.2005

Samin JC, Fisette P (2003) Symbolic Modeling of Multibody Systems. No. 112 in Solid Mechanics and Its Applications, Springer

Sardain P, Bessonnet G (2004) Zero Moment Point - Measurements From a Human Walker Wearing Robot Feet as Shoes. IEEE Transactions on Systems, Man, and Cybernetics - Part A: Systems and Humans 34(5):638–648, DOI 10.1109/TSMCA.2004.832833

Schaal S (2007) The New Robotics-towards human-centered machines. HFSP journal 1(2):115–26, DOI 10.2976/1.2748612

Smith EP, Rose KA (1995) Model goodness-of-fit analysis using regression and related techniques. Ecological Modelling 77(1):49–64, DOI 10.1016/0304-3800(93)E0074-D

Song S, Geyer H (2015) A neural circuitry that emphasizes spinal feedback generates diverse behaviours of human locomotion. The Journal of physiology DOI 10.1113/JP270228

Stokes VP, Andersson C, Forssberg H (1989) Rotational and translational movement features of the pelvis and thorax during adult human locomotion. Journal of Biomechanics 22(1):43–50

Taga G (1994) Emergence of bipedal locomotion through entrainment among the neuro-musculo-skeletal system and the environment. Physica D: Nonlinear Phenomena 75(1-3):190–208, DOI 10.1016/0167-2789(94)90283-6

Tsagarakis N, Laffranchi M, Vanderborght B, Caldwell D (2009) A compact soft actuator unit for small scale human friendly robots. In: 2009 IEEE International Conference on Robotics and Automation, pp 4356–4362, DOI 10.1109/ROBOT.2009.5152496

Tsagarakis NG, Morfey S, Medrano Cerda G, Li Z, Caldwell DG (2013) COMpliant huMANoid COMAN: Optimal joint stiffness tuning for modal frequency control. In: Proceedings - IEEE International Conference on Robotics and Automation, pp 673–678

Van der Noot N, Colasanto L, Barrea A, van den Kieboom J, Ronsse R, Ijspeert AJ (2015a) Experimental validation of a bio-inspired controller for dynamic walking with a humanoid robot. In: 2015 IEEE/RSJ International Conference on Intelligent Robots and Systems (IROS), pp 393–400, DOI 10.1109/IROS.2015.7353403

Van der Noot N, Ijspeert AJ, Ronsse R (2015b) Biped gait controller for large speed variations, combining reflexes and a central pattern generator in a neuromuscular model. In: 2015 IEEE International Conference on Robotics and Automation (ICRA), Seattle, WA, pp 6267–6274, DOI 10.1109/ICRA.2015.7140079

Van der Noot N, Ijspeert AJ, Ronsse R (2018) Bio-inspired controller achieving forward speed modulation with a 3d bipedal walker. The International Journal of Robotics Research 37(1):168–196, DOI 10.1177/0278364917743320

Vukobratovic M, Borovac B (2004) Zero-Moment Point - Thirty five years of its life. International Journal of Humanoid Robotics 01(01):157–173, DOI 10.1142/S0219843604000083

Wang JM, Hamner SR, Delp SL, Koltun V (2012) Optimizing locomotion controllers using biologically-based actuators and objectives. ACM Trans Graph p 25

Winter DA (1995) Anatomy, biomechanics and control of balance during standing and walking. Waterloo, Canada: Waterloo Biomechanics

Zobova AA, Habra T, Van der Noot N, Dallali H, Tsagarakis NG, Fisette P, Ronsse R (2017) Multiphysics modelling of a compliant humanoid robot. Multibody System Dynamics 39(1-2):95–114, DOI 10.1007/s11044-016-9545-4